



Efficient ionization of two-dimensional excitons by intense single-cycle terahertz pulsesHøgne C. Kamban * and Thomas G. Pedersen *Department of Materials and Production, Aalborg University, DK-9220 Aalborg Øst, Denmark
and Center for Nanostructured Graphene (CNG), DK-9220 Aalborg Øst, Denmark*

(Received 12 August 2021; revised 6 December 2021; accepted 7 December 2021; published 20 December 2021)

External electric fields are highly attractive for dynamical manipulation of excitons in two-dimensional materials. Here, we theoretically study the ionization of excitons in monolayer transition metal dichalcogenides (TMDs) by intense pulsed electric fields in the terahertz (THz) regime. We find that THz pulses with realistic field strengths are capable of ionizing a significant fraction of photogenerated excitons in TMDs into free charge carriers. Short THz pulses are therefore an efficient, noninvasive method of dynamically controlling the free carrier concentration in monolayer TMDs, which is useful for applications such as THz modulators. We further demonstrate that exciton ionization probabilities should be experimentally measurable by comparing free carrier absorption before and after the THz pulse. Detailed results are provided for different TMDs in various dielectric environments.

DOI: [10.1103/PhysRevB.104.235305](https://doi.org/10.1103/PhysRevB.104.235305)**I. INTRODUCTION**

Monolayer transition metal dichalcogenides (TMDs) are exciting materials for optoelectronic applications [1,2]. They are promising components in applications such as photodetectors [3–5], THz modulators [6,7], and solar cells [8,9], where they can absorb up to 5–10% of incident sunlight in a thickness less than 1 nm [8]. One of the most important characteristics of monolayer TMDs is the strongly bound excitons that form due to confinement and reduced screening in two-dimensional (2D) materials [10–12]. The optical properties of 2D materials are completely dominated by these excitons [10,13–15], and methods of manipulating them are therefore highly sought after. These methods may be as simple as altering the structural design of the device components by controlling, e.g., substrate screening. However, a major disadvantage with these approaches is that the properties are fixed once the components have been constructed. A more attractive option is therefore to control the properties using external fields that may be switched on or off at will and thereby obtain dynamic control of the material properties.

In recent years, interest in applying static in-plane electric fields to excitons in TMD monolayers, multilayers, and van der Waals heterostructures has been increasing [16–22]. This process induces excitons to ionize into free electrons and holes. Recently, this was observed in photocurrent measurements on WSe₂ [18]. The authors of Ref. [18] found an increase in the photoresponse rate as a function of field strength that was well explained by exciton ionization. However, to apply the electric field, the authors of Ref. [18] incorporated buried electrical contacts with a tiny gap into their TMD sample. This is by no means a trivial task, as it involves making complicated modifications to the sample.

Consequently, static electric fields become less attractive as a means of manipulating excitons.

With the rapid progression of THz technology, it is natural to ask how efficient pulsed THz electric fields are at inducing exciton ionization. A significant advantage of using THz pulses rather than static fields for this purpose is that no modifications need to be made to the sample. Whereas THz induced ionization of atoms in gaseous samples is typically measured by counting the number of ions produced during the pulse [23,24], the solid-state equivalent is typically discussed in electroabsorption experiments [25–27]. In these experiments, the absorption spectrum of a sample is measured in the presence of an electric field. In this case, one finds a shift and broadening of the exciton absorption peaks that depend on the strength of the electric field. The shift is well explained by the exciton Stark effect [17,28–30], while the broadening is commonly attributed to the reduced exciton lifetime due to field-induced exciton ionization [26,31,32]. However, detailed interpretations of recent electroabsorption experiments on both monolayer MoS₂ [33] and carbon nanotubes [34] reveal that exciton ionization is not the dominating contribution to this broadening. The authors of Refs. [33,34] base their arguments on the fact that the measured broadening is proportional to the square of the electric field strength, which is not predicted by exciton ionization [18,20]. The apparent contradiction is resolved by noting that the contribution to the broadening by exciton ionization alone [16,18,20] is much lower than the field-induced phonon contribution [33]. As a result, it is very difficult to measure exciton ionization rates in electroabsorption experiments.

In the present paper, we theoretically study exciton ionization in two-dimensional TMDs induced by intense single-cycle THz pulses. We find that nearly all ionization occurs within a very short time interval near the peak field strength of the THz pulse. For the longest pulse duration considered here, this ionization interval is about 0.5 ps, which

*hck@mp.aau.dk

is much shorter than the typical field-free exciton lifetimes of a few to hundreds of picoseconds in the popular TMDs WS₂ [35], WSe₂ [18,36,37], and MoS₂ [38,39]. We further show that a THz pulse with realistic field strength is capable of transforming a considerable portion of photogenerated excitons into free charge carriers in monolayer TMDs. This process happens over just a few picoseconds and therefore suggests that THz pulses are remarkably efficient for obtaining dynamic control over the number of free charge carriers, which is highly relevant for applications such as THz modulators [6,7]. Additionally, such a substantial change in the number of free charge carriers should be measurable in the free carrier absorption of a sample, or by collection via biased contacts, providing a direct method of estimating the exciton ionization probabilities in experiments. Our analysis clearly demonstrates that THz ionization of excitons in two-dimensional materials is feasible, and we provide quantitative estimates of the yield. To the best of our knowledge, previous works do not consider these phenomena and we hope our results will inspire attempts at experimental verification.

II. SIMULATION DETAILS

Within the two-band, effective mass approximation, excitons in a 2D TMD may be described by the two-dimensional Wannier equation [40,41], which has been shown to accurately reproduce exciton binding energies computed by more numerically demanding methods in various 2D materials [42–44]. In terms of the relative exciton coordinate $\mathbf{r} = \mathbf{r}_e - \mathbf{r}_h$, it reads (atomic units are used throughout)

$$\left[-\frac{1}{2\mu} \nabla^2 + V(\mathbf{r}) \right] \varphi_{mn}(\mathbf{r}) = E_{mn} \varphi_{mn}(\mathbf{r}), \quad (1)$$

where μ is the reduced exciton mass, V the interaction potential, and m and n denote the angular and principle quantum number, respectively. Due to cylindrical symmetry, angular momentum is a good quantum number in the Wannier model in the unperturbed case. In the present paper, we are interested in TMDs surrounded by in-plane isotropic media with dielectric tensor $\varepsilon_{a/b} = \text{diag}(\varepsilon_x^{(a/b)}, \varepsilon_x^{(a/b)}, \varepsilon_z^{(a/b)})$ above (a) and below (b) the sheet, respectively. The dielectric function of the encapsulated TMD may be approximated by a linearized form $\varepsilon(\mathbf{q}) = \kappa + r_0 q$, where \mathbf{q} is the momentum space coordinate, $\kappa = (\sqrt{\varepsilon_x^{(a)} \varepsilon_z^{(a)}} + \sqrt{\varepsilon_x^{(b)} \varepsilon_z^{(b)}})/2$ is the average dielectric constant between the sub- and superstrate [45,46], and the screening length r_0 is related to the polarizability of the TMD monolayer by $r_0 = 2\pi\alpha_{2D}$ [45,47]. In this case, V is given by the Rytova-Keldysh form [45,46,48,49]

$$V(\mathbf{r}) = -\frac{\pi}{2r_0} \left[H_0\left(\frac{\kappa r}{r_0}\right) - Y_0\left(\frac{\kappa r}{r_0}\right) \right], \quad (2)$$

where H_0 is the zeroth order Struve function and Y_0 the zeroth order Bessel function of the second kind [50]. We use the experimentally verified values for μ and r_0 from Ref. [51]. Additionally, when hBN surroundings are considered, we use the values for κ found in Ref. [51].

To study exciton ionization induced by THz pulses, a time-dependent dipole field term is included in the Wannier equation. We have obtained a trace of the experimental THz pulse used in Ref. [33], and the shape of the pulse used

throughout the present paper is based on this experimental pulse to ensure realistic simulations. It should be noted that this is only one of many possible pulse shapes. For instance, one could imagine using chirped pulses with a frequency content designed to ionize excitons through a sequence of transiently occupied excited states as an alternative. For performing computations, we assume that only the excitonic ground state is occupied initially and then let the wave function $\psi(t)$ evolve in time. The ionization probability P_{ion} is computed by subtracting the total occupation probability of all bound states P_{BS} from unity, i.e., $P_{\text{ion}}(t) = 1 - P_{\text{BS}}(t)$ where $P_{\text{BS}}(t) = \sum_b P_b(t)$. The bound states φ_b are the states with energy less than zero, and their occupation probabilities are given by $P_b = |\langle \varphi_b | \psi(t) \rangle|^2$. In order to get accurate ionization probabilities, we begin by studying excitons with an infinite field-free lifetime. That is, the only exciton removal mechanism is field-induced ionization. Note that the figures show the accumulated probability in contrast to the time resolved ionization rate, which roughly follows the pulse shape and, therefore, dies out after the pulse subsides. In Sec. IV, other mechanisms required for a realistic dynamical model will be included. In particular, excitons may reform from free carriers leading to re-establishment of equilibrium exciton concentrations after the THz pulse. Numerical computations are made feasible by forcing the wave functions to zero outside a large radius and external complex scaling is used to avoid spurious reflections from the boundary [20,52,53]. Further computational details may be found in Appendix A.

Figure 1(a) shows a schematic illustration of the exciton dynamics during the THz pulse. It may be divided into three temporal regions: (i) The exciton is initially in its unperturbed ground state. (ii) When the pulse is close to its peak field strength, the electron and hole are pulled in opposite directions. It is in this region that the vast majority of ionization occurs [54]. (iii) As the pulse subsides, the exciton has probabilities P_{ion} and $1 - P_{\text{ion}}$ of being in an ionized and bound state, respectively. Traces of the experimental and fitted THz pulses used in the simulations are shown in Fig. 1(b). Here, the black circles represent the experimental THz pulse obtained from the authors of Ref. [33]. To ensure easy reproducibility of the results, we introduce a fitted pulse with a simple functional form. This pulse is represented by the red line in Fig. 1(b), and it is justified by noting that the results obtained using both pulses are in excellent agreement. A simple functional form also has the advantage of making simulation of time propagation easier. The functional form is motivated by Ref. [55] and is given by $\mathcal{E}(t) = -\frac{\partial A(t)}{\partial t}$, where the vector potential reads

$$A(t) = -\frac{\mathcal{E}_0 \tau}{c} \exp \left\{ \left[\frac{1}{a} \tanh\left(\frac{bt}{\tau}\right) - 5^2 \right] \frac{t^2}{\tau^2} \right\}. \quad (3)$$

Here, \mathcal{E}_0 is the peak field strength, and a and b dictate the shape of the pulse. In the present paper, we choose $a = 0.12$ and $b = 3$ to accurately reproduce the main features of the experimental pulse. The coefficient c is chosen such that the peak field strength becomes \mathcal{E}_0 . We define the pulse duration to be from the moment it reaches 1% of its peak field strength to the moment it again reduces to 1% as it subsides. This duration is approximately τ . To approximate the experimental

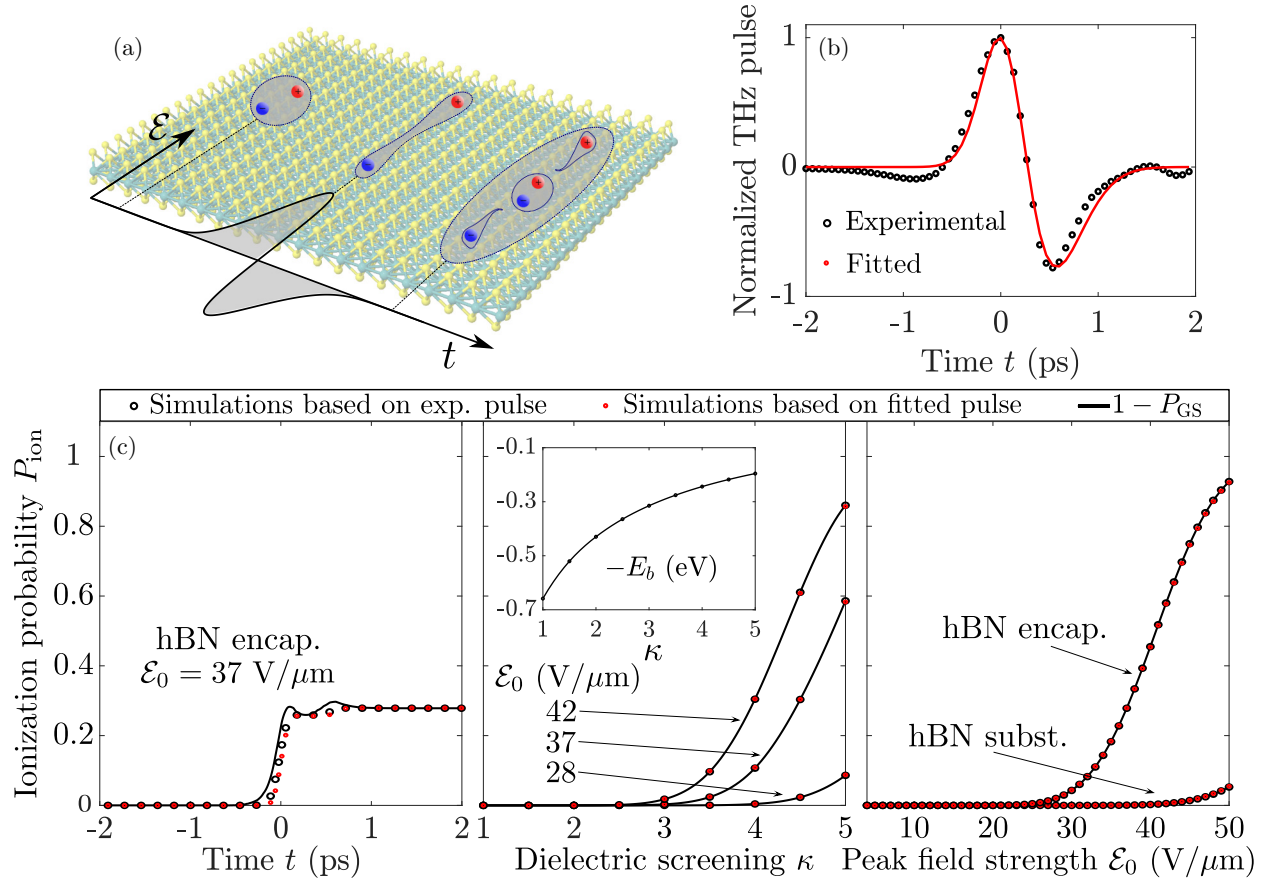


FIG. 1. (a) Schematic illustration of an exciton in a THz pulse. The initially bound exciton is polarized as a result of the pulse and is in a superposition of bound and ionized states as the pulse subsides. (b) Traces of the experimental pulse in Ref. [33] and the fitted pulse in Eq. (3) are shown as the black circles and red curve, respectively. Figure (c) summarizes the results for a single noninteracting exciton with an infinite field-free lifetime in MoS₂ subjected to the THz pulses in (b) with the black and red circles representing experimental and fitted pulses, respectively. The solid lines show the probability of depleting the ground state. (Left) Time-resolved exciton ionization probability during the THz pulse with a peak field strength of 37 V/ μm in hBN-encapsulated MoS₂. (Middle) Exciton ionization probabilities after the pulse for three different field strengths as functions of the dielectric surroundings. The inset shows the corresponding binding energies. (Right) Ionization probabilities after the pulse as functions of peak field strength for MoS₂ encapsulated by hBN as well as for MoS₂ on an hBN substrate.

pulse, we initially set $\tau = 2.1$ ps and later investigate changes in P_{ion} as τ is varied. Also, in all time-resolved results below, we shift the t axis such that the pulse reaches its peak value at $t = 0$.

III. RESULTS

Figure 1(c) summarizes the results for a single noninteracting exciton with an infinite field-free lifetime in MoS₂ exposed to a THz pulse. The three panels show the time-resolved ionization probability during the pulse (left), as well as the ionization probability after the pulse as a function of dielectric screening (middle) and peak field strength (right). In these panels, the black and red circles represent ionization probabilities P_{ion} obtained by using the experimental and fitted THz pulses, respectively, while the solid black lines show the ground state depletion probability $1 - P_{\text{GS}}$. The left panel reveals that the dynamics in the fitted and experimental THz pulses agree. Furthermore, while the ground state depletion probability and ionization probability do not coincide during

the pulse, they do when the pulse subsides. This indicates that excited states, that are completely ionized when the pulse has died out, are transiently occupied during the pulse. The dynamics are similar to those in Ref. [25], where exciton occupation probabilities in quantum-well structures subjected to THz radiation were investigated. The middle panel in Fig. 1(c) shows ionization probabilities after the pulse has died out (i.e., $t = 2$ ps) for three different peak field strengths as functions of surrounding dielectric screening κ . We again observe that $1 - P_{\text{GS}}$ and P_{ion} coincide after the pulse. This is a clear indication that the process is adiabatic, and the same conclusion was reached in Ref. [33]. Comparing the ionization probability with the binding energies for the relevant dielectric screening shown in the inset, we see that the increasing ionization probability is well explained by the reduced binding energy. In fact, ionization rates depend exponentially on the binding energies [22,56]. Common dielectric surroundings include SiO₂ substrates ($\kappa \approx 2.4$) and hBN encapsulation ($\kappa \approx 4.5$).

The right panel of Fig. 1(c) shows ionization probabilities as functions of peak field strength \mathcal{E}_0 for MoS₂ in two different

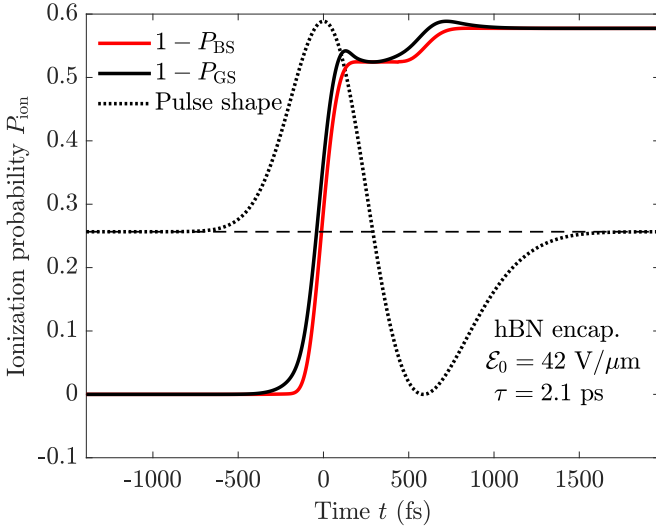


FIG. 2. Time-resolved ionization (red) and ground state depletion (black) probabilities for excitons in hBN-encapsulated MoS₂. The pulse shape is shown as the dotted line and is centered in time at its peak value of 42 V/μm with the dashed line indicating vanishing electric field level. The pulse duration is $\tau = 2.1$ ps.

dielectric surroundings. It is clear that the increased screening from encapsulating the TMD sheet in hBN, as opposed to simply placing it on an hBN substrate, causes a substantial increase in ionization probability. These results suggest that a single experimental THz pulse of the form used in Ref. [33] with a peak field strength of 42 V/μm would be able to ionize about 58% of the excitons in hBN-encapsulated MoS₂ where almost all of the ionization occurs over an interval of less than 0.5 ps (see Fig. 2). In their experiment, the authors of Ref. [33] use a sapphire substrate, which leads to an exciton binding energy of around 240 meV [33]. The authors find a broadening of the exciton absorption peak of about 10.8 meV for a peak field strength of 37 V/μm. In our calculations, this binding energy is reproduced by letting $\kappa \approx 4.1$. The middle panel of Fig. 1(c) reveals that about 14% of the excitons should be ionized in this case. This corroborates the assumption made by the authors that exciton ionization may be neglected compared to field-induced phonon broadening. The broadening induced by ionization alone may be estimated by using a static electric field of 37 V/μm. In this case, a full width of about 0.6 meV is found [20], further confirming that mechanisms other than exciton ionization dominate the broadening of the absorption peaks in this experiment. We note in passing that the results of Fig. 1(c) should not be compared directly to the absorption measurements in Ref. [33]. Intricate interplay between excitons and free charge carriers is important in realistic semiconductors and will be explored in Sec. IV.

To better understand the exciton dynamics in hBN-encapsulated MoS₂ subjected to a pulse of the experimental form in Ref. [33] with a peak field strength of 42 V/μm, we plot the time-resolved ionization rate in Fig. 2. It is evident that all ionization occurs over a remarkably short interval of about 0.5 ps. The reason for this is that the ionization rate depends exponentially on the field strength [20], and the

ionization rates at the tails of the THz pulse are therefore negligible.

The optimal material for a particular device is typically determined by requirements such as sensitivity to a certain wavelength. This is the case for, e.g., photodetectors, and it is therefore useful to have results for various materials that absorb light at different wavelengths. Figure 3 shows ionization probabilities in the four TMDs (a) MoS₂, (b) MoSe₂, (c) WS₂, and (d) WSe₂. The inset shows the exciton binding energies of these TMDs in the relevant range of dielectric surroundings. Common to all TMDs considered, hardly any ionization occurs if either the peak field strength is lower than 20 V/μm or the dielectric screening constant is close to unity (freely suspended). As the field strength and screening increase, a pronounced increase in ionization probability is observed. It is immediately clear that the tungsten based materials have larger ionization probabilities than molybdenum based ones in the relevant regions for device components. This is due to the lower exciton binding energies in the former, which suggests that it is easier to manipulate the free carrier density in these materials. If we consider the case with $\kappa = 3$ and $\mathcal{E}_0 = 40$ V/μm as an example, we see that when ordered from highest to lowest ionization probability, the four are WSe₂, followed by WS₂, MoS₂, and MoSe₂. This is in good agreement with the binding energies at $\kappa = 3$, for which we find $E_b^{(\text{MoSe}_2)} > E_b^{(\text{MoS}_2)} > E_b^{(\text{WS}_2)} > E_b^{(\text{WSe}_2)}$. Note that MoS₂ has a larger exciton binding energy than MoSe₂ for $\kappa \lesssim 2.5$ so that their binding energy curves cross. This is because MoS₂ has a lower 2D sheet polarizability than MoSe₂ [51]. However, as the surrounding dielectric screening is increased, the polarizability of the TMD sheet itself becomes less important and the larger reduced mass of the MoSe₂ excitons begins to dominate.

IV. FREE CARRIER DENSITY

To estimate the effect of a THz pulse on the free carrier concentration in a realistic TMD, one must take into account different loss mechanisms such as exciton recombination, exciton-exciton annihilation, and free carrier lifetimes, as well as impact ionization. To accurately include such effects, sophisticated theoretical modeling is often used [54]. In the present paper, the main focus is on obtaining an accurate prediction of ionization probabilities. However, it is interesting to see the effect that exciton ionization has on the free carrier concentration. To this end, we develop a simple model consisting of two coupled rate equations that describe the exciton n_x and free carrier n concentrations. Without external perturbations, we may write the coupled rate equations as

$$\frac{dn_x}{dt} = -\frac{n_x}{\tau_{\text{therm}}} + \gamma_c n^2 - \gamma_l n n_x, \quad (4)$$

$$\frac{dn}{dt} = \frac{n_x}{\tau_{\text{therm}}} - \gamma_c n^2 + \gamma_l n n_x. \quad (5)$$

Here, τ_{therm} is the exciton ionization rate due to thermal agitation, γ_c is the rate at which free electrons and holes combine to form excitons, and γ_l is the impact ionization rate, i.e., the rate at which excitons are ionized due to collisions with free carriers. For hBN-encapsulated WSe₂, a value of $\tau_{\text{therm}} \approx 100$ ps may be used [57]. The quantities γ_l and γ_c are

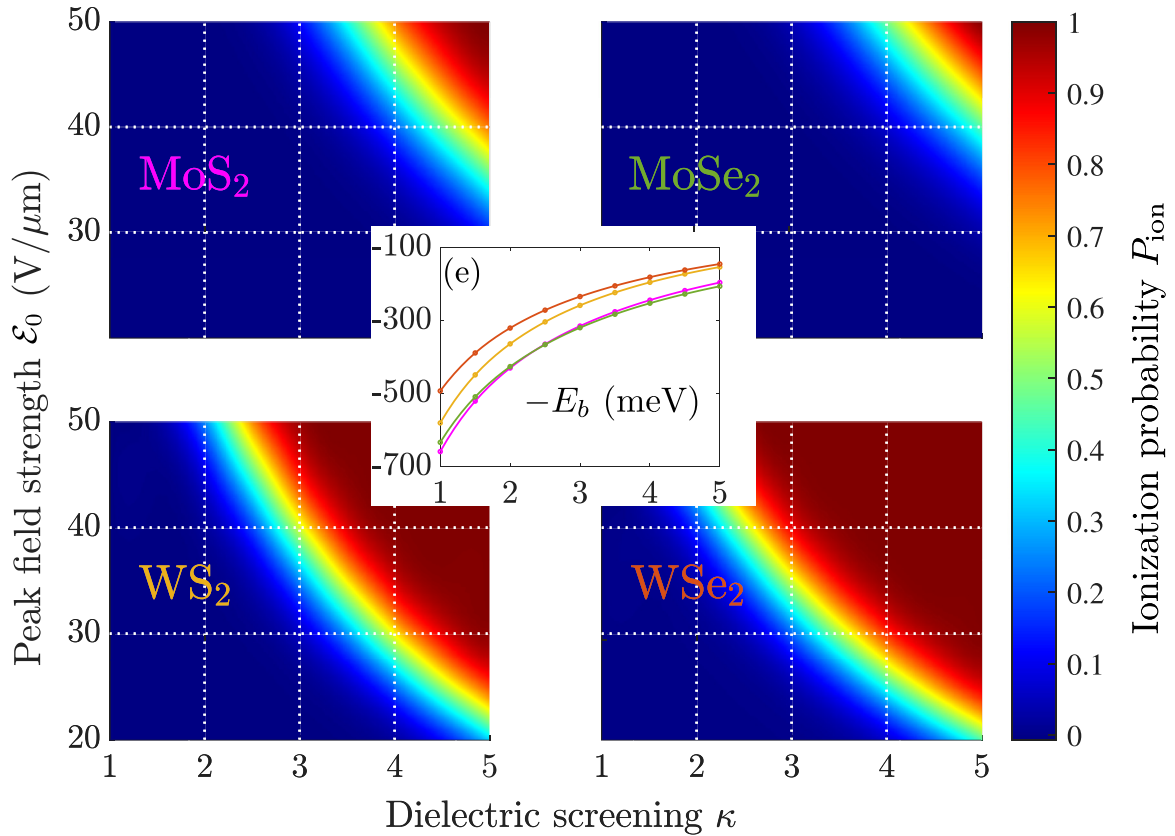


FIG. 3. Ionization probability as a function of peak field strength and surrounding dielectric screening for (a) MoS₂, (b) MoSe₂, (c) WS₂, and (d) WSe₂. Panel (e) shows the relevant binding energies. The colors of the TMD chemical composition in panels (a)–(d) correspond to the colors in panel (e).

estimated in Appendix B where we find $\gamma_I \approx 0.0043 \text{ cm}^2/\text{s}$ and $\gamma_c \approx 59 \text{ cm}^2/\text{s}$, respectively. Note that while a constant γ_I is used here, a THz field will accelerate free carriers which, in turn, increases impact ionization. As the acceleration depends on the field strength, γ_I will become time dependent. In our model, this may be simulated by changing the effective temperature. However, a slight change in γ_I does not alter the results much, and it will, therefore, be taken to be constant for simplicity.

In a realistic system, a laser pump is usually used to generate excitons. Furthermore, the excitons and free carriers have finite field-free lifetimes. To describe such a system, subjected to a THz pulse, one may write

$$\frac{dn_x}{dt} = G(t) + \left(\frac{d \log P_{BS}}{dt} - \frac{1}{\tau_x} - \frac{1}{\tau_{\text{therm}}} \right) n_x - \gamma_{ee} n_x^2 + \gamma_c n^2 - \gamma_I n n_x, \quad (6)$$

$$\frac{dn}{dt} = -\frac{n}{\tau_{fc}} + \left(\frac{1}{\tau_{\text{therm}}} - \frac{d \log P_{BS}}{dt} \right) n_x - \gamma_c n^2 + \gamma_I n n_x. \quad (7)$$

Here, $G(t)$ is the exciton generation rate, τ_x is the field-free exciton lifetime, γ_{ee} is the exciton-exciton annihilation rate, and τ_{fc} is the field-free free carrier lifetime. The logarithmic derivative of the total bound-state probability $P_{BS}(t)$ may be understood as a time-dependent ionization rate due to the applied THz pulse [53]. We use a linear interpolation of the

discrete bound-state probability found by the procedure in Appendix A to get a continuous P_{BS} . The coupled differential equations 6 and 7 may then be solved (starting from the equilibrium solutions) by a number of different methods. Here, we use the explicit Runge-Kutta (4,5) scheme that is built into MATLAB. Note that $d \log P_{BS}/dt$ depends on the field strength $\mathcal{E}(t)$ and is zero when $\mathcal{E} = 0$.

To describe the representative case of hBN-encapsulated WSe₂, we use $\tau_x \approx 90 \text{ ps}$ [36], $\gamma_{ee} \approx 0.05 \text{ cm}^2/\text{s}$ [18,37], and $\tau_{fc} \approx 40 \text{ ps}$ [58] together with the previously found quantities. We also assume a constant exciton generation rate $G = 2.5 \times 10^{24} \text{ s}^{-1} \text{ cm}^{-2}$ due to an external laser pump. The value is chosen such that we obtain the same equilibrium exciton density as used in Ref. [18]. We find initial equilibrium values of $n_x \approx 7 \times 10^{12} \text{ cm}^{-2}$ and $n \approx 3.5 \times 10^{10} \text{ cm}^{-2}$. The simulation results are shown in Fig. 4(a) with black and red curves representing the exciton and free carrier densities (left axis), respectively. The densities are initially assumed to be in statistical equilibrium, and a THz pulse reaching its peak field strength of $42 \text{ V}/\mu\text{m}$ at $t = 0$ is then turned on. This pulse is shown as the dotted black curve in Fig. 4(a) with absolute field strength shown on the right axis. A rapid increase in free carrier concentration from the initial $3.5 \times 10^{10} \text{ cm}^{-2}$ at equilibrium to about $1.8 \times 10^{12} \text{ cm}^{-2}$ can be observed. This is an increase in free carrier concentration by a factor of about 50 over a very short interval. After this sudden increase, the concentrations return to their equilibrium values almost instantaneously. It is evident that the densities are modified only

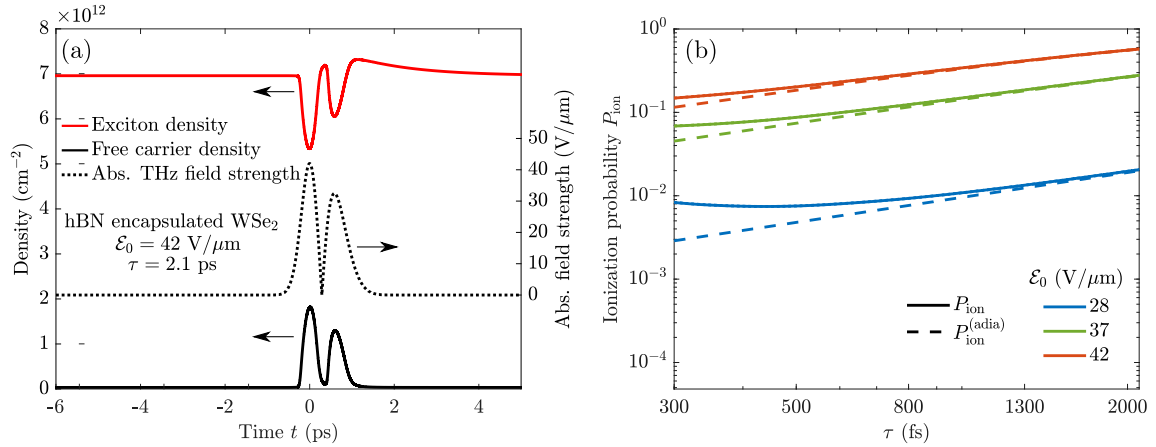


FIG. 4. (a) Exciton and free carrier densities in hBN-encapsulated WSe₂ obtained by solving the coupled rate equations (see Appendix B). The black and red curves indicate the exciton n_x and free carrier n densities (left axis), respectively. The densities are initially in equilibrium, that is $n_x \approx 7 \times 10^{12} \text{ cm}^{-2}$ and $n \approx 3.5 \times 10^{10} \text{ cm}^{-2}$. A THz pulse with a duration $\tau = 2.1$ ps reaching its peak field strength of $42 \text{ V}/\mu\text{m}$ at $t = 0$ is later turned on. The absolute THz field strength is shown as the black dotted curve (right axis). Realistic results are obtained by using a finite exciton generation rate and taking into account loss mechanisms from impurities (see Appendix B). (b) Ionization probability as a function of pulse duration for various peak field strengths, indicated by the different colors. The solid lines are the ionization P_{ion} probabilities computed by propagating the Wannier equation in time and projecting on the relevant bound states. The dashed lines are calculated using an adiabatic approach, utilizing the results from static electric fields. The adiabatic probabilities are given by $P_{\text{ion}}^{(\text{adia})} = 1 - e^{-\tau\Gamma_1}$, where $\Gamma_1 = \{9.62, 154.24, 407.63\} \text{ ns}^{-1}$ for $\mathcal{E}_0 = \{28, 37, 42\} \text{ V}/\mu\text{m}$, respectively. See Appendix C for details.

when the THz pulse is present. This ability to dynamically control the charge carrier concentration is very promising for applications such as THz modulators based on monolayer TMDs [6,7]. It should also make it possible to measure exciton ionization probabilities by correlating them to free carrier absorption spectra.

V. SHORTER PULSES

So far we have only considered THz pulses with duration given by $\tau = 2.1$ ps, closely resembling the experimental pulse used in Ref. [33]. For such relatively large τ the results are very accurately reproduced by adiabatic calculations, and it is therefore interesting to see how the results differ for shorter pulses. If the pulse varies sufficiently slowly in time, the adiabatic theorem allows us to obtain the ionization probability by treating time as a parameter in the time-dependent Hamiltonian. That is, one may increase the time parameter by small discrete steps, while repeatedly solving the resulting eigenvalue problem. This lets us trace the ground state energy and therefore the ionization probability. A detailed explanation of the procedure may be found in Appendix C. The results are summarized in Fig. 4(b), where we show the ionization probability of an exciton in MoS₂ encapsulated by hBN after the pulse has died out as a function of the pulse duration. The pulses considered are of the same shape as before but with a shorter duration. Different peak field strengths are indicated by line color. The solid lines show the ionization probabilities computed by propagating the Wannier equation in time (see Appendix A), while the dashed lines show adiabatic approximations (see Appendix C). We observe that for the longest pulses considered, the adiabatic calculation accurately reproduces the full time propagated results. Furthermore, we find that the ground state depletion probability and the ioniza-

tion probability are graphically indistinguishable for all pulse lengths shown in Fig. 4(b). This suggests that the excited states that are transiently occupied during the THz pulse are completely ionized once the pulse dies out. As the duration of the pulse decreases, we observe a deviation from the adiabatic results. This is to be expected, as the coupling between the states and the pulse should cease to be adiabatic for pulses that vary more rapidly with time. The results indicate that if the goal is to ionize as many excitons as possible, a pulse in the THz region is preferable over shorter pulses. The experimental THz pulse in Ref. [33] corresponds to the longest duration in Fig. 4(b) and therefore seems to be a good candidate for exciton ionization.

VI. SUMMARY

In summary, we have demonstrated using theoretical tools that realistic THz pulses may be used to efficiently ionize excitons in TMD monolayers, a desirable feature in many optoelectronic devices, such as photodetectors and THz modulators. We have shown that for the technologically important case of hBN-encapsulated MoS₂, a THz pulse with a peak field strength of $42 \text{ V}/\mu\text{m}$ (as applied in recent experiments [33]) will ionize about 58% of the photogenerated excitons. Reducing the peak field strength to $30 \text{ V}/\mu\text{m}$ already lowers the ionization probability to about 4.5%, revealing the extreme sensitivity to field strength. Similar behavior was demonstrated for MoSe₂, whereas exciton ionization probabilities in WS₂ and WSe₂ were shown to be considerably larger owing to their reduced exciton binding energies. In fact, a peak field of $30 \text{ V}/\mu\text{m}$ should ionize about 96% of the excitons in hBN-encapsulated WSe₂.

By solving the coupled rate equations for the exciton and free carrier concentrations in a realistic 2D semiconductor,

we have demonstrated that THz pulses boost the free carrier concentration considerably over a short time interval, providing dynamical control over both bound and free charge carriers. For the representative case of hBN-encapsulated WSe₂, we found an increase in free carrier concentration by about a factor 50. As the free carrier absorption is directly related to the number of free charge carriers, exciton ionization probabilities should be experimentally measurable in these materials by comparing free carrier absorption before and after the THz pulse or by collection via biased contacts. Finally, we have shown that reducing the duration of the pulse leads to ionization dynamics that are no longer adiabatic.

APPENDIX A: WANNIER EXCITONS IN THZ ELECTRIC FIELDS

To study exciton ionization induced by THz pulses, we include a time-dependent electric field term in the Wannier equation. Working in the length gauge under the dipole approximation and letting the field direction be along the x axis, we write

$$i \frac{\partial \psi(\mathbf{r}, t)}{\partial t} = H(t) \psi(\mathbf{r}, t), \quad (\text{A1})$$

with

$$H(t) = -\frac{1}{2\mu} \nabla^2 + V(\mathbf{r}) + \mathcal{E}(t)x, \quad (\text{A2})$$

where $\mathcal{E}(t)$ is the time-dependent field strength of the THz pulse. We will assume that only the excitonic ground state is occupied initially and then propagate Eq. (A1) in time while computing the ionization probability P_{ion} as

$$P_{\text{ion}}(t) = 1 - \sum_{m,n \text{ bound}} |\langle \varphi_{mn}(\mathbf{r}) | \psi(\mathbf{r}, t) \rangle|^2, \quad (\text{A3})$$

where we only count bound state solutions φ_{mn} of Eq. (1) (i.e., states with $E_{mn} < 0$). Note that $\sum_{m,n \text{ bound}} |\langle \varphi_{mn}(\mathbf{r}) | \psi(\mathbf{r}, t) \rangle|^2$ is equal to $P_{\text{BS}}(t)$ in the main text.

To perform numerical computations, the spatial region is truncated by placing the system inside a large radial box such that the wave function is forced to zero outside a radius R . This corresponds to introducing an infinite potential outside R . The wave function should be well described within this box as long as R is chosen large enough. Importantly, this allows us to write the wave function as a superposition of the *discrete* eigenstate solutions φ_{mn} to the unperturbed problem in Eq. (1) subject to $\varphi_{mn}(\mathbf{r}) = 0$ for $r \geq R$. We write

$$\psi(\mathbf{r}, t) = \sum_{m=0}^M \sum_{n=0}^N c_{mn}(t) \varphi_{mn}(\mathbf{r}) e^{-iE_{mn}t}, \quad (\text{A4})$$

with time-dependent expansion coefficients. In practical calculations, one must make sure that the results are converged in M , N , and R . We have used $R = 5000$ a.u. for our calculations (M and N are discussed later). Substituting Eq. (A4) into Eq. (A1), the following expression may be derived

$$\frac{d}{dt} c_{mn}(t) = -i \sum_{m'n'} c_{m'n'}(t) \mathcal{E}(t) \langle \varphi_{mn} | x | \varphi_{m'n'} \rangle \times e^{-i(E_{m'n'} - E_{mn})t}. \quad (\text{A5})$$

Thus, the expansion coefficients may easily be propagated in time, and the occupation probability of state φ_{mn} obtained as $|c_{mn}|^2$. An adaptive step-size eighth-order Dormand-Prince Runge-Kutta method with embedded fifth- and third-order methods for error control [59] has been used for time propagation.

The unperturbed states and energies have been obtained by expanding the eigenstates in a finite element (FE) basis

$$\varphi_{mn}(\mathbf{r}) = \sum_{k=1}^K \sum_{i=1}^p d_i^{(m,n,k)} f_i^{(k)}(r) \cos(m\theta), \quad (\text{A6})$$

where θ is the relative polar angle between the electron and hole, and k and i denote the radial segment and basis function, respectively. The procedure of using an FE approach to solve the Wannier equation is detailed in Ref. [20]. Nevertheless, a short explanation will now be given for completeness. Note that only the $\cos(m\theta)$ angular functions with $m \geq 0$ appear, as the electric field is taken along the x direction such that $x = r \cos \theta$. The radial functions $f_i^{(k)}$ are nonzero only on a specific radial segment $[r_{k-1}, r_k]$. On this segment, they are given by

$$f_i^{(k)}(r) = \frac{1}{2} [1 - y_k(r)] \delta_{i,1} + \frac{1}{2} [1 + y_k(r)] \delta_{i,p} + \frac{1}{2} \{ 2P_i[y_k(r)] + (-1)^{i+1} [1 - y_k(r)] - [1 + y_k(r)] \} \times (1 - \delta_{i,1} - \delta_{i,p}), \quad (\text{A7})$$

where δ is the Kronecker delta, P_i is the i th Legendre polynomial, and y_k maps the segment $[r_{k-1}, r_k]$ onto $[-1, 1]$

$$y_k(r) = \frac{2r - r_k - r_{k-1}}{r_k - r_{k-1}}. \quad (\text{A8})$$

This form ensures that all functions are zero at the segment boundaries with two exceptions, namely, the first and last function are equal to unity at the start and end of the segment, respectively. That is,

$$f_i^{(k)}(r_{k-1}) = f_i^{(k)}(r_k) = 0, \quad (\text{A9})$$

$$\text{except } f_1^{(k)}(r_{k-1}) = f_p^{(k)}(r_k) = 1. \quad (\text{A10})$$

This makes it simple to guarantee continuity of the wave function, even if the FE functions themselves are discontinuous, by requiring that $c_p^{(k-1)} = c_1^{(k)}$. This can be done by, e.g., grouping the two relevant functions into a single function so that they have the same expansion coefficient. Furthermore, forcing the wave function to zero at R is achieved by omitting the final function on the final segment. Substituting the expansion in Eq. (A6) into Eq. (1) and taking the inner product with $f_i^{(k')} \cos(m'\theta)$, one may construct a matrix eigenvalue problem that determines the states $\varphi_{m,n}$ in terms of the FE coefficients $d_i^{(m,n,k)}$. Once these coefficients are obtained, they may be used to propagate Eq. (A5) in time. With the above procedure, it is the limits K and p that determine the number of unperturbed states N for a given angular quantum number m . In our computations, we have made sure that the results are converged and have used $K = 80$, $p = 30$, and $M = 16$. We have furthermore excluded states in the pseudocontinuum with energy larger than 20 eV to improve numerical stability.

One of the advantages of using an FE expansion is that it is easy to implement exterior complex scaling (ECS) outside a particular radius R_0 chosen such that $R_0 < R$. In this region $r \geq R_0$, one lets the radial coordinate rotate into the complex plane

$$r \rightarrow \begin{cases} r & \text{for } r < R_0 \\ R_0 + (r - R_0)e^{i\phi} & \text{for } r > R_0, \end{cases} \quad (\text{A11})$$

by an angle ϕ (we use $\phi = 0.4$). This reduces the amount of spurious reflections from the boundary considerably, and greatly reduces the number of pseudocontinuous states necessary for convergences [52,60]. The ECS formalism is related to the uniform complex scaling (UCS) formalism, which is well explained in Ref. [61]. Here, one lets the radial coordinate rotate into the complex plane in the entire region ($R_0 = 0$), i.e., $r \rightarrow re^{i\phi}$. The UCS formalism is applicable whenever the potential is dilation analytic (i.e., it can be expanded in a Taylor series) [62]. ECS has been used in cases where UCS fails [63]. When they both are applicable, which is the case for the RK potential, they yield (formally) identical eigenvalues [64]. Under the transformation, the bound state energies remain real, while the continuous states are rotated into the complex plane, where they obtain a negative imaginary part [64]. This imaginary part turns oscillating continuous states into exponentially decaying states for $r > R_0$. The spectrum of complex eigenstates is still complete [62]. The exponential decay improves the numerical stability of the expansion in Eq. (A4) by reducing spurious reflections when we force the states to zero at $r = R$. While the two procedures should lead to identical results formally, we found the ECS approach to be more numerically stable when propagated in time. ECS is implemented in the above procedure by using the transformed Hamiltonian and integration path according to Eq. (A11) in inner products corresponding to segments with $r > R_0$. In our calculations, we have used $R_0 = 4937.5$ a.u. such that it coincides with the start of the final segment.

APPENDIX B: IMPACT IONIZATION AND EXCITON FORMATION RATES

The impact ionization rate γ_I may be estimated by [65]

$$\gamma_I = \int_0^\infty D(E)v(E)\sigma_I(E)dE, \quad (\text{B1})$$

where D is the energy distribution, v the free carrier velocity, and σ_I the exciton impact ionization cross section. In an effective mass approximation, we have $E = k^2/2m_e$ with the effective electron mass $m_e = 0.45$ [66]. We assume the energy distribution to be Maxwellian $D(E) = \exp(-E/k_B T)/k_B T$, where k_B is the Boltzmann constant and T the electron temperature. Note that the electron temperature is not necessarily the same as the surrounding temperature and that $\int_0^\infty D(E)dE = 1$. In Ref. [65] it was found that

$$\sigma_I \approx \frac{16}{k_0} \left(\frac{k_0^2}{k^2} - \frac{k_0^4}{k^4} \right) \theta(k - k_0), \quad (\text{B2})$$

which has a maximum of $4/k_0$, where k_0 is defined in terms of $E_b = k_0^2/2m_e$. Approximating the scattering cross section by

its maximum, it is found that

$$\gamma_I \approx \frac{1}{m_e} \left[2\sqrt{\frac{\pi}{z}} \Phi_c(\sqrt{z}) + 4e^{-z} \right], \quad (\text{B3})$$

where $z = E_b/k_B T$ and Φ_c is the complementary error function. Using an exciton binding energy of $E_b = 161.4$ meV and assuming the electron temperature is $T = 300$ K, a value of $\gamma_I \approx 0.0043$ cm²/s is found. It should be noted that using a slightly higher temperature does not have a large impact on the value of γ_I . To estimate the rate at which electrons and holes combine to form excitons γ_c , we will use the Saha equation, which describes the free carrier and exciton densities after statistical equilibration of their chemical potentials in the Boltzmann limit [67]

$$\frac{n^2}{n_x} = \frac{k_B T \mu}{2\pi} e^{-E_b/k_B T}. \quad (\text{B4})$$

The equilibrium solutions are obtained by setting the first order derivatives in Eqs. 4 and 5 equal to zero and supplementing with Eq. (B4) to determine γ_c . Here, we find $\gamma_c \approx 59$ cm²/s.

APPENDIX C: ADIABATIC IONIZATION PROBABILITY

Assuming that the system is initially in its (nondegenerate) ground state φ_{GS} , and that $\mathcal{E}(t)$ varies sufficiently slowly, the adiabatic theorem states that the system will remain in the eigenstate of $H(t)$ that evolves from the initial state φ_{GS} . This allows us to find the energy at all times by treating time as a parameter and tracing the relevant state. That is, we find the eigenstates of $H(t')$ at a time t'

$$H(t')\varphi_\lambda(\mathbf{r}; t') = E_\lambda(t')\varphi_\lambda(\mathbf{r}; t'), \quad (\text{C1})$$

where E and φ depend on t' as a parameter. Then we let t' take on values from the initial to the final t , all the while keeping track of the state that evolves from the ground state. Using the complex scaling procedure [20], we are then able to obtain both the real (Stark shift) and imaginary (ionization rate) part of the energy. The relevant (adiabatic) state is

$$\psi(\mathbf{r}, t) = \exp\left\{-i \int_{-\infty}^t E(t')dt'\right\} \varphi_{GS}(\mathbf{r}; t). \quad (\text{C2})$$

As the pulse subsides, ψ will return to the ground state $c\varphi_{GS}(\mathbf{r}) \exp(-iE_{GS}t)$, where c is a complex number that arises from the integral in Eq. (C2), resulting in a norm less than unity. Defining the ionization rate as $\Gamma = -2\text{Im} E$, we obtain the adiabatic ionization probability

$$P_{\text{ion}}^{(\text{adia})}(t) = 1 - \exp\left\{-\int_{-\infty}^t \Gamma(t')dt'\right\}. \quad (\text{C3})$$

Note that the pulse in Eq. (1) in the main text depends only on τ as the fraction t/τ . We therefore have

$$\Gamma(t; \tau, \mathcal{E}_0) = \Gamma\left(\frac{t}{\tau}; 1, \mathcal{E}_0\right) \quad (\text{C4})$$

and

$$\int_{-\infty}^{\infty} \Gamma(t')dt' = \tau\Gamma_1, \quad (\text{C5})$$

where

$$\Gamma_1 = \int_{-\infty}^{\infty} \Gamma(t'; 1, \mathcal{E}_0) dt'. \quad (\text{C6})$$

The adiabatic ionization probability after the pulse is therefore

$$P_{\text{ion}}^{(\text{adia})}(t \rightarrow \infty) = 1 - \exp(-\tau \Gamma_1). \quad (\text{C7})$$

- [1] J. R. Schaibley, H. Yu, G. Clark, P. Rivera, J. S. Ross, K. L. Seyler, W. Yao, and X. Xu, Valleytronics in 2D materials, *Nat. Rev. Mater.* **1**, 16055 (2016).
- [2] C. Gong, Y. Zhang, W. Chen, J. Chu, T. Lei, J. Pu, L. Dai, C. Wu, Y. Cheng, T. Zhai, L. Li, and J. Xiong, Electronic and optoelectronic applications based on 2D novel anisotropic transition metal dichalcogenides, *Adv. Sci.* **4**, 1700231 (2017).
- [3] Z. Yin, H. Li, H. Li, L. Jiang, Y. Shi, Y. Sun, G. Lu, Q. Zhang, X. Chen, and H. Zhang, Single-layer MoS₂ phototransistors, *ACS Nano* **6**, 74 (2012).
- [4] O. Lopez-Sanchez, D. Lembke, M. Kayci, A. Radenovic, and A. Kis, Ultrasensitive photodetectors based on monolayer MoS₂, *Nat. Nanotechnol.* **8**, 497 (2013).
- [5] H. Wang, C. Zhang, W. Chan, S. Tiwari, and F. Rana, Ultrafast response of monolayer molybdenum disulfide photodetectors, *Nat. Commun.* **6**, 8831 (2015).
- [6] Y. Cao, S. Gan, Z. Geng, J. Liu, Y. Yang, Q. Bao, and H. Chen, Optically tuned terahertz modulator based on annealed multilayer MoS₂, *Sci. Rep.* **6**, 22899 (2016).
- [7] Z. Fan, Z. Geng, W. Fang, X. Lv, Y. Su, S. Wang, J. Liu, and H. Chen, Characteristics of transition metal dichalcogenides in optical pumped modulator of terahertz wave, *AIP Adv.* **10**, 045304 (2020).
- [8] M. Bernardi, M. Palumbo, and J. C. Grossman, Extraordinary sunlight absorption and one nanometer thick photovoltaics using two-dimensional monolayer materials, *Nano Lett.* **13**, 3664 (2013).
- [9] O. Lopez-Sanchez, E. Alarcon Llado, V. Koman, A. Fontcuberta I Morral, A. Radenovic, and A. Kis, Light generation and harvesting in a van der Waals heterostructure, *ACS Nano* **8**, 3042 (2014).
- [10] A. Ramasubramanian, Large excitonic effects in monolayers of molybdenum and tungsten dichalcogenides, *Phys. Rev. B* **86**, 115409 (2012).
- [11] T. C. Berkelbach, M. S. Hybertsen, and D. R. Reichman, Theory of neutral and charged excitons in monolayer transition metal dichalcogenides, *Phys. Rev. B* **88**, 045318 (2013).
- [12] T. Olsen, S. Latini, F. Rasmussen, and K. S. Thygesen, Simple Screened Hydrogen Model of Excitons in Two-Dimensional Materials, *Phys. Rev. Lett.* **116**, 056401 (2016).
- [13] Q. H. Wang, K. Kalantar-Zadeh, A. Kis, J. N. Coleman, and M. S. Strano, Electronics and optoelectronics of two-dimensional transition metal dichalcogenides, *Nat. Nanotechnol.* **7**, 699 (2012).
- [14] D. Y. Qiu, F. H. da Jornada, and S. G. Louie, Optical Spectrum of MoS₂: Many-Body Effects and Diversity of Exciton States, *Phys. Rev. Lett.* **111**, 216805 (2013).
- [15] M. L. Trolle, G. Seifert, and T. G. Pedersen, Theory of excitonic second-harmonic generation in monolayer MoS₂, *Phys. Rev. B* **89**, 235410 (2014).
- [16] S. Hastrup, S. Latini, K. Bolotin, and K. S. Thygesen, Stark shift and electric-field-induced dissociation of excitons in monolayer MoS₂ and hBN/MoS₂ heterostructures, *Phys. Rev. B* **94**, 041401(R) (2016).
- [17] B. Scharf, T. Frank, M. Gmitra, J. Fabian, I. Žutić, and V. Perebeinos, Excitonic Stark effect in MoS₂ monolayers, *Phys. Rev. B* **94**, 245434 (2016).
- [18] M. Massicotte, F. Vialla, P. Schmidt, M. B. Lundeberg, S. Latini, S. Hastrup, M. Danovich, D. Davydovskaya, K. Watanabe, T. Taniguchi, V. I. Fal'ko, K. S. Thygesen, T. G. Pedersen, and F. H. Koppens, Dissociation of two-dimensional excitons in monolayer WSe₂, *Nat. Commun.* **9**, 1633 (2018).
- [19] A. R. Klots, A. K. Newaz, B. Wang, D. Prasai, H. Krzyzanowska, J. Lin, D. Caudel, N. J. Ghimire, J. Yan, B. L. Ivanov, K. A. Velizhanin, A. Burger, D. G. Mandrus, N. H. Tolk, S. T. Pantelides, and K. I. Bolotin, Probing excitonic states in suspended two-dimensional semiconductors by photocurrent spectroscopy, *Sci. Rep.* **4**, 6608 (2014).
- [20] H. C. Kamban and T. G. Pedersen, Field-induced dissociation of two-dimensional excitons in transition metal dichalcogenides, *Phys. Rev. B* **100**, 045307 (2019).
- [21] T. G. Pedersen, S. Latini, K. S. Thygesen, H. Mera, and B. K. Nikolić, Exciton ionization in multilayer transition-metal dichalcogenides, *New J. Phys.* **18**, 073043 (2016).
- [22] H. C. Kamban and T. G. Pedersen, Interlayer excitons in van der Waals heterostructures: Binding energy, Stark shift, and field-induced dissociation, *Sci. Rep.* **10**, 5537 (2020).
- [23] R. R. Jones, D. You, and P. H. Bucksbaum, Ionization of Rydberg Atoms by Subpicosecond Half-Cycle Electromagnetic Pulses, *Phys. Rev. Lett.* **70**, 1236 (1993).
- [24] S. Li and R. R. Jones, Ionization of Excited Atoms by Intense Single-Cycle THz Pulses, *Phys. Rev. Lett.* **112**, 143006 (2014).
- [25] B. Ewers, N. S. Köster, R. Woscholski, M. Koch, S. Chatterjee, G. Khitrova, H. M. Gibbs, A. C. Klettke, M. Kira, and S. W. Koch, Ionization of coherent excitons by strong terahertz fields, *Phys. Rev. B* **85**, 075307 (2012).
- [26] M. Stein, C. Lammers, J. T. Steiner, P. H. Richter, S. W. Koch, M. Koch, and M. Kira, Exciton ionization by THz pulses in germanium, *J. Phys. B: At. Mol. Opt. Phys.* **51**, 154001 (2018).
- [27] Y. Murotani, M. Takayama, F. Sekiguchi, C. Kim, H. Akiyama, and R. Shimano, Terahertz field-induced ionization and perturbed free induction decay of excitons in bulk GaAs, *J. Phys. D: Appl. Phys.* **51**, 114001 (2018).
- [28] J. Klein, J. Wierzbowski, A. Regler, J. Becker, F. Heimbach, K. Müller, M. Kaniber, and J. J. Finley, Stark effect spectroscopy of mono- and few-layer MoS₂, *Nano Lett.* **16**, 1554 (2016).
- [29] T. G. Pedersen, Exciton Stark shift and electroabsorption in monolayer transition-metal dichalcogenides, *Phys. Rev. B* **94**, 125424 (2016).
- [30] L. S. R. Cavalcante, D. R. da Costa, G. A. Farias, D. R. Reichman, and A. Chaves, Stark shift of excitons and trions in two-dimensional materials, *Phys. Rev. B* **98**, 245309 (2018).
- [31] J. D. Dow and D. Redfield, Electroabsorption in semiconductors: The excitonic absorption edge, *Phys. Rev. B* **1**, 3358 (1970).

- [32] D. A. B. Miller, D. S. Chemla, T. C. Damen, A. C. Gossard, W. Wiegmann, T. H. Wood, and C. A. Burrus, Electric field dependence of optical absorption near the band gap of quantum-well structures, *Phys. Rev. B* **32**, 1043 (1985).
- [33] J. Shi, E. Baldini, S. Latini, S. A. Sato, Y. Zhang, B. C. Pein, P. C. Shen, J. Kong, A. Rubio, N. Gedik, and K. A. Nelson, Room temperature terahertz electroabsorption modulation by excitons in monolayer transition metal dichalcogenides, *Nano Lett.* **20**, 5214 (2020).
- [34] T. Ogawa, S. Watanabe, N. Minami, and R. Shimano, Room temperature terahertz electro-optic modulation by excitons in carbon nanotubes, *Appl. Phys. Lett.* **97**, 041111 (2010).
- [35] L. Yuan and L. Huang, Exciton dynamics and annihilation in WS₂ 2D semiconductors, *Nanoscale* **7**, 7402 (2015).
- [36] F. Cadiz, C. Robert, E. Courtade, M. Manca, L. Martinelli, T. Taniguchi, K. Watanabe, T. Amand, A. C. Rowe, D. Paget, B. Urbaszek, and X. Marie, Exciton diffusion in WSe₂ monolayers embedded in a van der Waals heterostructure, *Appl. Phys. Lett.* **112**, 152106 (2018).
- [37] S. Mouri, Y. Miyauchi, M. Toh, W. Zhao, G. Eda, and K. Matsuda, Nonlinear photoluminescence in atomically thin layered WSe₂ arising from diffusion-assisted exciton-exciton annihilation, *Phys. Rev. B* **90**, 155449 (2014).
- [38] H. Shi, R. Yan, S. Bertolazzi, J. Brivio, B. Gao, A. Kis, D. Jena, H. G. Xing, and L. Huang, Exciton dynamics in suspended monolayer and few-layer MoS₂ 2D crystals, *ACS Nano* **7**, 1072 (2013).
- [39] T. Korn, S. Heydrich, M. Hirmer, J. Schmutzler, and C. Schller, Low-temperature photocarrier dynamics in monolayer MoS₂, *Appl. Phys. Lett.* **99**, 102109 (2011).
- [40] G. H. Wannier, The structure of electronic excitation levels in insulating crystals, *Phys. Rev.* **52**, 191 (1937).
- [41] F. L. Lederman and J. D. Dow, Theory of electroabsorption by anisotropic and layered semiconductors. I. Two-dimensional excitons in a uniform electric field, *Phys. Rev. B* **13**, 1633 (1976).
- [42] P. Cudazzo, C. Attaccalite, I. V. Tokatly, and A. Rubio, Strong Charge-Transfer Excitonic Effects and the Bose-Einstein Exciton Condensate in Graphane, *Phys. Rev. Lett.* **104**, 226804 (2010).
- [43] O. Pulci, P. Gori, M. Marsili, V. Garbuio, R. Del Sole, and F. Bechstedt, Strong excitons in novel two-dimensional crystals: Silicane and germanane, *Europhys. Lett.* **98**, 37004 (2012).
- [44] S. Latini, T. Olsen, and K. S. Thygesen, Excitons in van der Waals heterostructures: The important role of dielectric screening, *Phys. Rev. B* **92**, 245123 (2015).
- [45] M. L. Trolle, T. G. Pedersen, and V. Véniard, Model dielectric function for 2D semiconductors including substrate screening, *Sci. Rep.* **7**, 39844 (2017).
- [46] H. C. Kamban, T. G. Pedersen, and N. M. R. Peres, Anisotropic Stark shift, field-induced dissociation, and electroabsorption of excitons in phosphorene, *Phys. Rev. B* **102**, 115305 (2020).
- [47] P. Cudazzo, I. V. Tokatly, and A. Rubio, Dielectric screening in two-dimensional insulators: Implications for excitonic and impurity states in graphane, *Phys. Rev. B* **84**, 085406 (2011).
- [48] N. S. Rytova, The screened potential of a point charge in a thin film, *Moscow Univ. Phys. Bull.* **22**, 18 (1967).
- [49] L. V. Keldysh, Coulomb interaction in thin semiconductor and semimetal films, *JETP Lett.* **29**, 658 (1979).
- [50] M. Abramowitz and I. Stegun, eds., *Handbook of Mathematical Functions, With Formulas, Graphs, and Mathematical Tables* (Dover, New York, 1972).
- [51] M. Goryca, J. Li, A. V. Stier, T. Taniguchi, K. Watanabe, E. Courtade, S. Shree, C. Robert, B. Urbaszek, X. Marie, and S. A. Crooker, Revealing exciton masses and dielectric properties of monolayer semiconductors with high magnetic fields, *Nat. Commun.* **10**, 4172 (2019).
- [52] A. Scrinzi, Infinite-range exterior complex scaling as a perfect absorber in time-dependent problems, *Phys. Rev. A* **81**, 053845 (2010).
- [53] H. C. Kamban, S. S. Christensen, T. Søndergaard, and T. G. Pedersen, Finite-difference time-domain simulation of strong-field ionization: A perfectly matched layer approach, *Phys. Status Solidi B* **257**, 1900467 (2020).
- [54] F. Langer, C. P. Schmid, S. Schlauderer, M. Gmitra, J. Fabian, P. Nagler, C. Schüller, T. Korn, P. G. Hawkins, J. T. Steiner, U. Huttner, S. W. Koch, M. Kira, and R. Huber, Lightwave valleytronics in a monolayer of tungsten diselenide, *Nature (London)* **557**, 76 (2018).
- [55] B. C. Yang and F. Robicieux, Field-ionization threshold and its induced ionization-window phenomenon for Rydberg atoms in a short single-cycle pulse, *Phys. Rev. A* **90**, 063413 (2014).
- [56] J. C. G. Henriques, H. C. Kamban, T. G. Pedersen, and N. M. R. Peres, Analytical quantitative semiclassical approach to the Lo Surdo-Stark effect and ionization in two-dimensional excitons, *Phys. Rev. B* **102**, 035402 (2020).
- [57] R. Perea-Causín, S. Brem, and E. Malic, Phonon-assisted exciton dissociation in transition metal dichalcogenides, *Nanoscale* **13**, 1884 (2021).
- [58] G. Aivazian, H. Yu, S. Wu, J. Yan, D. G. Mandrus, D. Cobden, W. Yao, and X. Xu, Many-body effects in nonlinear optical responses of 2D layered semiconductors, *2D Mater.* **4**, 025024 (2017).
- [59] W. H. Press, S. A. Teukolsky, W. T. Vetterling, and B. P. Flannery, *Numerical Recipes*, 3rd ed. (Cambridge University Press, New York, 2007).
- [60] J. Bengtsson, E. Lindroth, and S. Selstø, Solution of the time-dependent Schrödinger equation using uniform complex scaling, *Phys. Rev. A* **78**, 032502 (2008).
- [61] J. Bengtsson, *On the use of the uniform complex scaling-method for studying time-dependent systems* (Department of Physics, Stockholm University, 2012), p. 58.
- [62] N. Moiseyev, *Non-Hermitian Quantum Mechanics* (Cambridge University Press, Cambridge, 2011).
- [63] B. Simon, The definition of molecular resonance curves by the method of exterior complex scaling, *Phys. Lett. A* **71**, 211 (1979).
- [64] C. W. McCurdy, C. K. Stroud, and M. K. Wisinski, Solving the time-dependent Schrödinger equation using complex-coordinate contours, *Phys. Rev. A* **43**, 5980 (1991).
- [65] A. Dargys and J. Kundrotas, Impact ionization of excitons by hot carriers in quantum wells, *Semicond. Sci. Technol.* **13**, 1258 (1998).
- [66] S. Haastrup, M. Strange, M. Pandey, T. Deilmann, P. S. Schmidt, N. F. Hinsche, M. N. Gjerding, D. Torelli, P. M.

Larsen, A. C. Riis-Jensen, J. Gath, K. W. Jacobsen, J. J. Mortensen, T. Olsen, and K. S. Thygesen, The Computational 2D Materials Database: High-throughput modeling and discovery of atomically thin crystals, *2D Mater.* **5**, 042002 (2018).

[67] R. A. Kaindl, D. Hägele, M. A. Carnahan, and D. S. Chemla, Transient terahertz spectroscopy of excitons and unbound carriers in quasi-two-dimensional electron-hole gases, *Phys. Rev. B* **79**, 045320 (2009).